

On the power of data augmentation for head pose estimation

Michael Welter
Independent Researcher
michael@welter-4d.de

Abstract

Deep learning has been impressively successful in the last decade in predicting human head poses from monocular images. However, for in-the-wild inputs the research community relies predominantly on a single training set, 300W-LP, of semisynthetic nature without many alternatives. This paper focuses on gradual extension and improvement of the data to explore the performance achievable with augmentation and synthesis strategies further. Modeling-wise a novel multitask head/loss design which includes uncertainty estimation is proposed. Overall, the thus obtained models are small, efficient, suitable for full 6 DoF pose estimation, and exhibit very competitive accuracy.

1 Introduction

Human head pose estimation (HPE) is an important task in many application e.g. in the automotive sector or in entertainment products. The concrete problem addressed by this paper is monocular head pose estimation for in-the-wild scenarios, i.e. from given a facial crop a computer vision system must estimate the face orientation. Closely related is the task of face alignment where a mathematical description of a face is inferred, e.g. as landmarks or full 3D reconstruction. These tasks are particularly challenging due to the diversity and non-rigid nature of faces. However, in recent years deep learning methods have been very successful at it [3]. In HPE, the current state of the art achieves errors of ca. 3 (MAE) to 5° (geodesic) [6, 30].

The main interest behind this work lies in devising a simple, efficient and effective HPE model. Because the margin for model size and complexity is therefore limited, the choice of the training data is a knob left to turn freely. In this regard the goal this paper is exploration of this path toward further improvements of HPE models. Extension and combination of existing datasets, as well as augmentation is the means to this end which might also serve the community in the future with custom datasets. However, first we shall review related literature.

For in-the-wild HPE we can recognize two datasets as de facto standard: AFLW2000-3D and 300W-LP [56]. AFLW2000-3D, serving as test set, consists of 2000 images labeled with 6 DoF poses, parameters of deformable facial 3D model, as well as landmarks. The images are challenging due to occlusion, extreme poses and varying illumination. 300W-LP, commonly used as training data, similarly consists ca. 61 thousand labeled images. It was constructed by augmenting a smaller set of faces with out-of-plane rotations. Some authors [14] chose to expand this data further with fine-grained movements, or employ a face swapping augmentation [49]. However, the impact of this was not considered in isolation.

In contrast, the Biwi dataset [9], popular as another benchmark, comprises 24 sequences including extreme poses of 20 subjects in a laboratory environment. Interestingly, it is used in recent works [13, 25, 26] which train on fully synthetic images from the SynHead dataset [13]. They are however limited to the lab setting and a low number of individuals.

Regarding mathematical models for HPE, a baseline may consist of a learned feature extractor, such as a convolutional neural network and final linear layers which, after some simple transformation, output orientation, position, size and so on. Such a network could be trained with losses such as L1 or L2 penalizing the errors from the known ground truths. Various rotation representations have been introduced [6, 16, 19]. More sophisticated model architectures and loss calculations are proposed in [30, 42, 49]. The authors of [14] devised an algorithm switching between different losses dynamically. Multitask networks leveraging synergies between 3D HPE and 2D landmark prediction were considered in [47]. Competitive HPE results could also be achieved by suitably shaped, yet relatively simple loss functions [6].

Uncertainty estimation, while rarely addressed in the face analysis community [32], is potentially useful for filtering and outlier rejection. However, exploration downstream applications is beyond the scope of this paper. Ultimately, uncertainty estimation is included because it boosted the model's accuracy. For simplicity,

only aleathoric (data) uncertainty is modeled. This is implemented by outputting parameters for an assumed probability density of the data and taking its negative log likelihood as loss [23, 27]. In the space of rotations $SO(3)$ this is particularly challenging numerically, requiring e.g. normalization constants which do not have close-form expressions [8, 12, 36, 39, 52]. Here, this will be addressed by a tangent space formulation.

In short, the contributions of this paper are:

- A HPE model yielding improved accuracy over the current state of the art.
- Introduction of extended training data, including ablation studies.
- Novel multitask head/loss and data augmentation designs.
- A novel tangent-space approach for rotational uncertainty estimation.

While most ingredients are nothing new, their combination into competitive designs in the field of HPE is. The model was integrated into the FOSS OpenTrack¹, and will therefore be referred to as OpNet. The full source code for training and evaluation is available on github².

2 Methods

2.1 Model Design

The model architecture consists of a feature extraction backbone, global pooling, 50% dropout, and a linear layer per prediction head. The raw features of each head are mapped to final predicted quantities, respectively. As input, the model takes a 129×129 monochrome face crop. The motivation for monochrome inputs is invariance to hue changes in the local illumination conditions. ResNet18 [15] and MobileNetV1 [18] were picked as feature extractors since they are lightweight and proved to work well on various tasks. To enable full 6 DoF tracking, and to enable learning from landmark-only annotations, the model has the following outputs: 3D rotation, 2D position and size, facial shape parameters, bounding box, and uncertainty parameters.

Rotations are represented by quaternions, which are suitable for limited range HPE [6], avoiding the gimbal-lock problem of Euler angles. Note that quaternions q and $-q$ represent the same orientation. Accuracy was better if this ambiguity was avoided and the network was biased toward identity output. Hence, the quaternion is formed from the feature $z_1 \dots z_4$ by

$q = q' / \|q'\|$, $q' = iz_1 + jz_2 + kz_3 + \text{smoothclip}(z_4)$, where i, j, k is the imaginary basis, $\text{smoothclip}(x) = \text{ELU}(x) + 1$ maps \mathbb{R} to \mathbb{R}^+ , and ELU is the function introduced in [5].

2D position and **size** are both estimated in image space, normalized to $[-1, 1]$. The 2D position is taken identically from the respective linear layer. The size feature is passed through smoothclip in order to guarantee a positive value.

The model outputs **shape parameters** for the Basel Face Model (BFM) [38] which consists of a 3D base-geometry modified by a combination of deformation basis vectors. Following the literature [14, 42, 49, 56, 57], the parameters are coefficients for 50 bases to realize different facial shapes and expressions. Only 68 points which make up the **3D landmarks** are actually computed. They adhere to the MultiPIE 68-point markup [35, 44].

The rationale for **bounding box** prediction is practicality, namely tracking the face through a video sequence as in the demo from [14]. The output is parameterized by center and size, where the size-features are mapped by smoothclip to positive values.

Rotation uncertainty is considered in the tangent-space of rotations $\mathfrak{so}(3)$ which essentially encodes offsets from a particular orientation by rotation vectors. Thus, the data variation around the predicted pose can be described by a standard multivariate normal distribution. To eliminate redundancy, the center of the distribution is fixed at zero. It has been shown that for small variance this formulation approximates a distribution on $SO(3)$ asymptotically [28, 29, 52].

Consequently, we must parameterize a covariance matrix Σ . To this end, the network outputs a lower triangular matrix $\mathbf{M} \in \mathbb{R}^{3 \times 3}$ filled with six features taken from a BatchNorm (BN) layer added after the final linear layer. Intuitively, BN helps decouple the learning of the magnitude of the variance from the influence of unrelated losses. Without it, the networks didn't perform well. Hence, given \mathbf{M} , the covariance matrix is set to $\Sigma = \mathbf{M}\mathbf{M}^T + \epsilon\mathbf{I}$ resembling a Cholesky decomposition, but the diagonals of \mathbf{M} do not need to be positive and the addition of \mathbf{I} scaled with a small constant ensures strict positivity. Note that $\mathbf{M}\mathbf{M}^T$ is symmetric positive semi-definite.

Position and size uncertainty is modeled by a 3D multivariate normal distribution for the triplet combining 2D position and head size. Its covariance matrix is constructed like in the case of rotations.

¹<https://github.com/opentrack/opentrack>

²<https://github.com/opentrack/neuralnet-tracker-traincode/tree/paper>

2.2 Losses

The training procedure minimizes the sum of individual losses, corresponding to the predicted quantities (in the following marked with hat $\hat{\cdot}$).

In general, mean and variance parameters $\hat{\mu}$ and $\hat{\sigma}$ are learned by minimizing the negative log likelihood (NLL), i.e. $-\log p(y|\hat{\mu}(x), \hat{\sigma}(x))$ of the data density p over some dataset consisting of input-output tuples (x, y) [23, 27]. Naive approaches have been reported as unstable [37, 45]. As remedy, an initial period where the variance is fixed was suggested. For historical reasons the present model is instead trained with a combination of traditional regression losses and NLL, and for "symmetry" reasons NLL losses are employed even for shape parameters, bounding box and landmarks, in case of which variances are learned as auxiliary parameters independent of the inputs.

For the **rotation** prediction we penalize the geodesic distance by the losses

$$L_{rot}(\hat{q}, q) = 1 - |\hat{q} \cdot q|^2 \quad (1)$$

$$NLL_{rot}(\hat{q}, q, \hat{\Sigma}_{rot}) = -\log f(Im \log(\hat{q}^{-1}q) | 0, \hat{\Sigma}_{rot}), \quad (2)$$

where L_{rot} was inspired by the metrics surveyed in [20]. The \cdot signifies the inner product of vectors. In NLL_{rot} , f denotes the probability density, \log returns an imaginary quaternion containing the rotation vector, from which Im extracts the imaginary part as 3d vector, the length of which is the geodesic distance, i.e. the smallest rotation magnitude between \hat{q} and q .

Furthermore, considering **position and size** stacked in a 3d vector p , the employed losses are L2 and NLL with the normal distribution with variance $\hat{\Sigma}_p$. We thus define

$$L_p(\hat{p}, p) = \|p - \hat{p}\|^2 \quad (3)$$

$$NLL_p(\hat{p}, p, \Sigma_p) = -\log f(p|\hat{p}, \Sigma_p). \quad (4)$$

The **shape parameters**, denoted ϕ_i , are assumed to be distributed independently normal. This simplifies the covariance to a diagonal matrix $\hat{\Sigma}_{shp} = \text{diag}(\sigma_1, \sigma_2, \dots)$. The corresponding losses are the L2 loss $L_\phi(\hat{\phi}, \phi)$ and NLL with normal distribution $NLL_\phi(\hat{\phi}, \phi, \hat{\Sigma}_\phi)$ which are defined analogously to Eq. (3) and Eq. (4), and omitted for brevity.

For **landmarks** the L1 loss worked well. The corresponding NLL is based on the Laplace distribution. Again, statistical independence is assumed. Then the total loss decomposes into sums over coordinate-wise contributions. Moreover, it is useful to apply weights w_i to different parts of the face. Thus, the losses are

defined by

$$L_\xi(\hat{\xi}, \xi) = \sum_i w_i |\xi_i - \hat{\xi}_i| \quad (5)$$

$$NLL_\xi(\hat{\xi}, \xi, \hat{\Sigma}_\xi) = -\sum_i w_i \log f_{Laplace}(\xi_i | \hat{\xi}_i, \hat{\sigma}_{\xi,i}), \quad (6)$$

where i runs over the 68×3 spatial landmark coordinates. If only x and y coordinates are available, then the summation runs only over those.

The **bounding box** is trained like the shape parameters using L2 loss L_{bb} and NLL_{bb} . Input to those losses are the box corner coordinates, assuming independence.

In order to encourage the network to output nearly unit quaternions, the term $L_{norm}(\hat{q}') = |1 - |\hat{q}'||^2$ is added, where \hat{q}' is the unnormalized quaternion.

At last we can define the total loss L by

$$L = L' + \beta_{total} NLL_{total} \quad (7)$$

$$L' = \alpha_{rot} L_{rot} + \alpha_p L_p + \alpha_\phi L_\phi \quad (8)$$

$$+ \alpha_\xi L_\xi + \alpha_{bb} L_{bb} + \alpha_{norm} L_{norm} \quad (9)$$

$$NLL_{total} = \beta_{rot} NLL_{rot} + \beta_p NLL_p + \beta_\phi NLL_\phi \quad (10)$$

$$+ \beta_\xi NLL_\xi + \beta_{bb} NLL_{bb}, \quad (11)$$

with weighting factors α and β .

2.3 Augmentations

Data samples consist of the input image, a 2D facial bounding box (BB), and the remaining labels. They are first subject to geometric transformations where also cropping to the face area is performed. In principle, a square region of interest (ROI) is generated initially from the BB extending its shortest side. This ROI is subsequently scaled, rotated, and translated by random amounts. Resampling this (rotated) square at the input resolution creates the face crop. Additionally, the crop is mirrored with probability $p = 1/2$ and rotated by 90° with $p = 1/100$. Note that no stretching occurs. Finally, the BB is regenerated by taking the BB around the transformed corner points.

Afterwards image intensity augmentations are applied³. This process is designed to occasionally produce strong distortions with the intent to facilitate generalization to overexposure, noisy low-light images and similar challenging inputs. First, from Equalize, Posterize, Gamma, Contrast, Brightness, and Blur, four are picked and applied with small probabilities up to $p = 1/10$ chance. Then Gaussian noise is randomly added with $p \approx 1/2$ and scale up to $\sigma = 16/256$ w.r.t. the normalized image intensity.

³Using the Kornia package <https://kornia.github.io/>

3 Datasets

Initially training was conducted on 300W-LP, however, performance turned out lacking and facial-expression dependent systematic pose errors were noticeable. Hypothetically, lacking diversity in 300W-LP might contribute to that, i.e. limited pitch range, uniform illumination and mostly open eyes. This motivated the creation of a new dataset, closely following the creation of 300W-LP which should address these shortcomings. Thereby only the out-of-plane rotation synthesis was performed using the original 300W-LP source images with their BFM parameters.

3.1 Extended 300W-LP Reproduction

Let’s consider the key ingredients. Firstly, the 3D face model. On the basis of same facial region of the BFM as in [14], a smooth transition to a background plane was modeled. The resulting mesh is shown in the Appendix Fig. 5. The deformation basis was extended to the new vertices by copying the vectors from the closest BFM vertex and attenuating them by a distance-dependent decay factor. To the original basis, new shapes with closed eyes were added. Given an input image, a depth profile is imposed on the background plane according to a monocular depth estimate. This is performed by an off-the-shelf MiDaS model ⁴ [40, 41]. Then, as in [56], a new image is generated by projecting the original image onto the 3D mesh, rotating the face together with the left or right half of the background, smoothly blending between transformed and pristine parts, and rendering the result. In addition to unlit renderings, some faces are lit from the side with probability 1/1000. Closed eyes are sampled with probability 1/2.

The Appendix contains comparisons with 300W-LP in Fig. 6. Furthermore, scatter plots of rotation distributions are depicted in Fig. 9. It shall be said that while useful, the novel eye and illumination additions are far from perfect. The eye regions suffer from small misalignment errors and the illumination suffers from shadow-mapping artifacts and generally does not look particularly realistic. The source code is available in a separate repository ⁵.

3.2 WFLW & LaPa Large Pose Extension

This section covers further expansion of the training data to in-the-wild images where no pose annotations

⁴MiDaS v3 - Hybrid, https://pytorch.org/hub/intelis1_midas_v2/

⁵<https://github.com/DaWelter/face-3d-rotation-augmentation>

are available. As an improvised solution, 2D landmark annotations were leveraged. Perfect labels are thereby not the goal but that the network could learn from relative differences between frames generated by out-of-plane rotations synthesis.

Inspired by the face-alignment methods [7, 11, 58, 58] (based on the FLAME head-model [31]), the general idea is to fit 3D landmarks of the BFM to the 2D annotations. Those methods incorporate also photometric fitting and other techniques. Here, to keep things simple and consistent with 2D, only the visible side of the BFM is used. Then indeed landmarks alone are not sufficient to identify plausible 3D reconstructions. To remedy this, initial guesses and pose priors were obtained from a small neural network ensemble trained without the extended data, and the space of possible shape parameters was soft-constrained by incorporating a NLL loss of a Gaussian mixture which was fitted to the shape parameters in the 300W-LP dataset. Ultimately, the labeling process consists of solving a standard minimization problem for the sum of several losses: landmark error, rotation error from the prior, the shape NLL, as well as soft-constraints for quaternion normalization and non-negative head-size. The result was manually curated, removing poorly fitted frames. Afterwards the rotation expansion from Sec. 3.1 was applied. Code and notebooks to reproduce every step is available in the source repository.

The procedure was applied to WFLW [50] and LaPa [33]. Appealing for this paper, they consist of facial images of a large variety of individuals, poses, and occlusions. WFLW comprises $7.5 \cdot 10^3$ training images with 98 manually annotated landmarks. The landmarks were converted to 68 points by interpolation. LaPa contains ca. $1.8 \cdot 10^4$ images annotated with 106 points. However, the latter includes images from 300W-LP which were excluded due to the overlap. The remaining images are from Megaface [22]. Ultimately, there were 4942 images from LaPa expanded to ca. $7.7 \cdot 10^4$, and 1554 images from WFLW expanded to ca. $2.2 \cdot 10^4$. The created datasets are provided online. Figure 7 and Fig. 8 in the Appendix show sample images.

3.3 Face Synthetics

The Face Synthetics (FS) dataset [48] consists of 10^5 fully synthetic, photorealistic, rendered human heads, annotated with segmentation masks and 3D landmarks. The subjects are composed of randomly sampled face shape, hairstyle, accessories, skin color, superimposed on a variety of backgrounds. Thus, the annotations are perfect and artifacts from 300W-LP-style out-of-plane rotations are absent. The authors provide only the 3D

landmarks and of those only the x and y coordinates. Therefore, only the corresponding landmark losses L_ξ and NLL_ξ are enabled. The facial bounding box is constructed based on the segmentation, encompassing pixels marked as "face" and "nose". Samples where a side length is less than 32 pixels are filtered out.

4 Implementation Details

The network is trained with the ADAM optimizer [24] for $N = 15\text{M}$ samples with a maximum learning (LR) rate of 10^{-3} . The LR ramps up for $N/20$ samples and decreases after $N/2$ samples to $1/10\text{th}$. After $2/3N$ samples, stochastic weight averaging [21] is enabled. Furthermore, gradient clipping with threshold 0.1 is used. Training time is a few hours on standard desktop hardware.

Facial BB's are often taken around the annotated landmarks [14, 42]. Here, they encompass the full reconstructed facial section of the BFM taken from [14] (using all of its vertices). In case of Biwi, which provides neither landmarks nor boxes, boxes are extracted from the annotations file provided with [6] and shrunk by 80%. As a result, the facial BB's are consistent across the 300W-LP family, AFLW2000-3D, Biwi and FS.

Regarding cropping, the scale factor determining the facial ROI is sampled from $\mathcal{N}(s, 0.1)$, with $s = 1.1$ and subsequently clipped to $[s - 0.5, s + 0.5]$. Next, consider the ROI translation after scaling. A maximum movement of $t = \frac{1}{2} \max(0, roi - bb) + \frac{1}{3} bb$ is allowed, where roi and bb stand in sloppy notation for the extent of the expanded ROI and the original box's side length, respectively. The concrete translation is sampled from $\mathcal{N}(0, t/2)$ and clipped to $[-t, t]$. This design allows some translation for zoomed-in crops and otherwise placement of the face anywhere in the crop such that 70% of the BB remains visible. The ROI rotation angle is sampled from a uniform distribution between -30 and 30° .

As intensity augmentation, noise is in fact potentially added twice, once with probability $p = 1/2$ and $\sigma = 4$ and secondly with $p = 0.1$ and $\sigma = 16$. This redundant application is implemented as such purely for convenience.

Multiple datasets are combined via simple random draws. First a dataset is picked with a certain frequency, followed by picking a sample from the dataset with replacement.

Regarding the landmark weights, eye centers (i.e. top and bottom, 8 point in total) are weighted with $w_i = 0$ since good samples with closed eyes are scarce. The loss weights are $\alpha_{rot} = 1, \alpha_p = 1, \alpha_\phi = 0.01, \alpha_\xi = 1, \alpha_{bb} = 0.01, \alpha_{norm} = 10^{-6}, \beta_{total} = 0.01$ to bring

the NLL range to the same order of magnitude as the other losses, $\beta_{rot} = 1, \beta_p = 1, \beta_\phi = 0.01, \beta_\xi = 1$ and $\beta_{bb} = 0.01$.

5 Results

The model was evaluated on AFLW2000-3D and Biwi introduced in Sec. 1. Furthermore, some ablation experiments were conducted as well as an analysis of the noise response and effectiveness of the uncertainty estimation.

Evaluations were performed on five different networks and the metrics were averaged. Reported are the absolute errors of Euler angles, the mean of those (MAE), as well as the average of the geodesic errors ($\|Im \log(\hat{q}^{-1}q)\|$). The largest observed standard error of the sample mean was 0.03° among all evaluations of AFLW2000-3D and 0.07° for Biwi.

The baseline (BL) was trained on the combination of custom large pose expansions of 300W-LP, WFLW and LaPa with sampling probabilities 50%, 33% and 16%, respectively. These frequencies were picked ad-hoc, guided by the size of the datasets, preliminary experiments, and the quality of the BFM fits. Optimizing them is left as potential future work. Later on Face Synthetics was added (BL + FS), using the frequencies 50% 300W-LP, 33.3% WFLW, 8.4% LaPa, and 8.4% FS. The low amount of FS samples was motivated by its fully synthetic nature and incomplete labels.

A perhaps notable aspect in this work is the consistent avoidance of stretching the input faces. For Biwi at least, it is common to extract and resize the area under the facial BB to the input size [6, 51]. Instead, consistent with training, the BB is first expanded to a square (and enlarged by 10%).

In the evaluation of AFLW2000-3D, the standard protocol in [43] was followed apart from the input crop, including the removal of 30 samples with yaw, pitch or roll angles larger than 99° . Table 1 shows a comparison with literature values. Evidently, the BL is already very accurate, yet adding FS, yielded further improvement from 3.19 to 3.15° MAE, improving over SOTA by over two sigmas.

The benchmarking on Biwi, the results of which are presented in Tab. 2, follows the experimental protocol from [51] (apart from the crop), and uses exactly the same frames and facial BB's as in [6]. Evaluations with the alignment strategy from [6] were also conducted, compensating for different camera angles and other biases between coordinate systems. Without it, results are modest. With alignment, the accuracy improves drastically. However, results for 6DRepNet are not readily available, and a re-evaluation was out-of-scope. Whether aligned results are representative of the true

performance can be questioned because as per [6] the alignment is performed on a per-sequence/individual basis, thus eliminating systematic biases caused by the subject’s appearance.

Table 1. Rotation errors in degrees from the AFLW2000-3D benchmark. YPR stands for yaw,pitch and roll, MAE for their average and Geo for the geodesic error.

Method	Y	P	R	MAE	Geo.
HopeNet [43]	6.47	6.56	5.44	6.15	9.93
FSA-Net [51]	4.50	6.08	4.64	5.07	8.16
WHENet [55]	4.44	5.75	4.31	4.83	-
TokenHPE [53]	4.36	5.54	4.08	4.66	-
QuatNet [19]	3.97	5.61	3.92	4.50	-
LSR [4]	3.81	5.42	4.00	4.41	-
MFDNet [32]	4.30	5.16	3.69	4.38	-
EHPNet [46]	3.23	5.54	3.88	4.15	-
6DRepNet [16]	3.63	4.91	3.37	3.97	-
img2pose [1]	3.42	5.03	3.27	3.91	6.41
6DoF-HPE [2]	3.56	4.74	3.35	3.88	-
MNN [47]	3.34	4.69	3.48	3.83	-
SADRNet [42]	3.93	5.00	3.54	3.82	-
DAD-3DHeads [34]	3.08	4.76	3.15	3.66	-
SynergyNet [49]	3.42	4.09	2.55	3.35	-
SRHP [6]	2.76	4.25	2.76	3.26	5.29
DSFNet [30]	2.65	4.28	2.82	3.25	-
OpNet BL	2.80	4.22	2.54	3.19	5.26
OpNet BL + FS	2.79	4.18	2.49	3.15	5.23

Table 2. Rotation errors from the Biwi benchmark.

Method	Y	P	R	MAE	Geo.
FSA-Net [51]	4.27	4.96	2.76	4.00	7.64
SRHP (6D) [6]	4.58	4.65	2.71	3.98	7.30
img2pose [1]	4.56	3.54	3.24	3.78	7.10
HopeNet [43]	4.53	3.08	2.83	3.48	6.60
WHENet [55]	3.60	4.10	2.73	3.48	-
6DRepNet [16]	3.24	4.48	2.68	3.47	-
6DRepNet360 [17]	3.37	3.87	2.93	3.39	-
OpNet BL	3.80	4.93	2.57	3.77	7.21
OpNet BL + FS	3.66	4.61	2.44	3.57	7.01
Aligned					
HopeNet [43]	4.53	3.08	2.83	3.48	6.60
img2pose [1]	4.04	3.12	3.03	3.40	6.23
SRHP (Euler) [6]	3.98	3.09	2.40	3.16	5.42
FSA-Net [51]	3.59	2.90	2.27	2.92	5.36
OpNet BL	2.84	2.75	2.90	2.83	5.01
OpNet BL + FS	2.57	2.47	2.92	2.65	4.72

Figure 1 visualizes the worst estimates judging by rotation error. It reveals failures in situations with heavy occlusion and a sample with two visible faces. It also shows apparently mislabeled samples where the predictions look more plausible.

Table 3 shows results from various method ablations. Increasing the backbone capacity from MobileNet to ResNet18 improved the metrics only insignificantly. Removal of landmark predictions yielded a small improvement in MAE over the BL. Hypothetically, synergetic effects between tasks did not occur in the BL and now more capacity was freed for pose prediction. However, the landmark prediction was needed to utilize the annotations of the Face Synthetics data. The variant without landmarks and ResNet backbone would have been very strong if only geodesic distance was considered but the MAE metric suffered so drastically that it cannot be considered the best. The other modifications worsened the accuracy in both metrics. Interestingly, in-plane rotation augmentation had a big impact, where a smaller rotation range yielded intermediate results.

Table 3. Ablation study with different variations of the methodology. Every line means a change from the baseline (OpNet BL). Changes are not cumulative with other lines. ResNet18 means the feature extractor was replaced with it. A minus means removal of the ingredient. "Intensity Aug." refers to the image intensity augmentations, "NLL" to the NLL losses, "Landmarks" to the landmark losses, "In-plane Rot." to the respective rotation augmentation, and "5° In-plane Rot." to overridden rotation limits.

Method Variation	MAE	Geo.
OpNet BL	3.19	5.26
ResNet18	3.18	5.24
- Landmarks	3.16	5.26
ResNet18 - Landmarks	3.27	5.21
- Intensity Aug.	3.24	5.37
- NLL	3.30	5.35
- In-plane Rot.	3.53	5.65
5° In-plane Rot.	3.44	5.56

Table 4 shows an ablation study for dataset variations. Starting from modest results with 300W-LP, the accuracy improves as more data is added. Interestingly, even the basic 300W-LP reproduction (R-300W-LP) improved performance. The reason is unknown, but it could be explained by a slightly different rotation distribution or the 3D geometry in particular due to the depth estimation. Adding directional lighting and closed eyes yielded a further boost.

Aside of benchmark outcomes, in practice the ResNet18 variant produced subjectively noticeably smoother predictions than the BL. This motivated an evaluation on noisy inputs, the results of which are shown in Figure 3. And indeed, as the noise is increased, the gap between rotation errors widens to ca 0.25° which might explain the subjective feeling. On the other hand this gap amounts to only 5% of the total error magnitude, so other aspects could play a role.

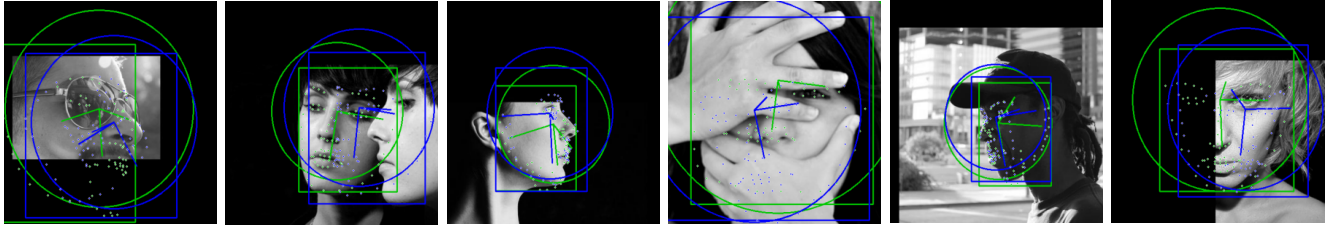


Figure 1. Visualization of the samples from AFLW2000-3D with the worst rotation error. Predictions are blue, ground truth is green. Shown are axes of the local coordinate system, landmarks and bounding box.



Figure 2. Visualization of the samples from Biwi with the worst rotation error, analogous to Fig. 1

Table 4. Ablation study with different training distributions. "300W-LP" refers to the original dataset, "FS" to Face Synthetics, "R-300W-LP" to the reproduction, "RA-300W-LP" the reproduction with closed eyes and profile illumination, and finally "EX" to the extension generated from LaPa and WFLW.

Notes	Dataset	MAE	Geo.
	300W-LP	3.44	5.44
	300W-LP + FS	3.34	5.36
	R-300W-LP	3.28	5.34
	RA-300W-LP	3.27	5.27
BL	RA-300W-LP + EX	3.19	5.26
BL + FS	RA-300W-LP + EX + FS	3.15	5.23

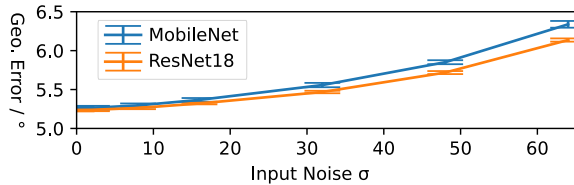


Figure 3. Plots the geodesic error of rotation predictions versus the standard deviation σ of Gaussian noise added to input images. The evaluations are conducted over AFLW2000-3D modified by noise. The error bars show the standard error of the sample mean over the five evaluation networks.

Figure 4 demonstrates some degree of effectiveness of the uncertainty estimation. Note that the failure cases with errors larger than 40° are correctly attributed with correspondingly large uncertainty. Overall the correlation between pose error and uncertainty is rather weak.

Since the network is equipped with a landmark pre-

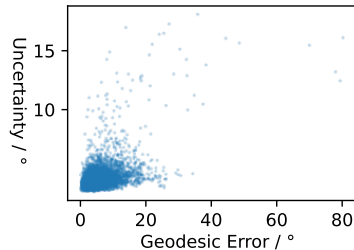


Figure 4. Correlation of the uncertainty estimate with rotation errors. The data points iterate over samples from AFLW2000 and the five BL evaluation networks. Recall that the uncertainty estimate $\hat{\Sigma}_{rot}$ is a covariance matrix. Plotted is its Frobenius norm to condense it to a single number.

diction head, it was also evaluated on the AFLW2000-3D sparse face alignment benchmark following the protocol in [56]. The metric thereof measures the distance of the 68 3D-landmarks from ground truth labels using the normalized mean absolute error of the x and y components (NME 2D), ignoring the depth coordinate. It is computed separately for three yaw bins, $[0^\circ, 30^\circ)$, $[30^\circ, 60^\circ)$ and $[60^\circ, 90^\circ)$. Respective results are presented in Tab. 5 together with literature values from prior art. As can be seen, the accuracy is decent but not up to current SOTA. However, OpNet was also not optimized for landmark prediction.

6 Conclusion

This work presents an approach to HPE which achieves highly competitive performance by leveraging data and data-augmentation strategies to much greater extend

Table 5. NME 2D evaluation on AFLW2000-3D. The middle three columns correspond to the yaw bins and "Mean" shows the average of the three.

Method	0-30	30-60	60-90	Mean
3DDFA [56]	3.78	4.54	7.93	5.42
PRNet [10]	2.75	3.51	4.61	3.62
3DDFA V2 [14]	2.63	3.42	4.48	3.51
SADRNet [42]	2.66	3.30	4.42	3.46
SynergyNet [49]	2.65	3.30	4.27	3.41
JVCR [54]	2.69	3.08	4.15	3.31
OpNet BL	2.80	3.54	4.43	3.59
OpNet BL + FS	2.75	3.48	4.41	3.55

than before. While none of the ideas are new, we can recognize the degree of their effectiveness.

The results suggest that out-of-plane rotation synthesis from [56] has not yet reached its limit, i.e. when slightly improved and applied to a sufficiently large and diverse data volume, significantly better performing models might be trained than with the original 300W-LP dataset. Adding a different flavor of synthetic data, namely the Face Synthetics can boost performance further, where potentially the different image style helps to overcome the domain gap to the real world. The extent of improvement is surprising since an otherwise moderately performing model is boosted to beyond SOTA with quite some margin.

On the other hand the approach in this work was not very effective for face alignment. The paper also does not address the question of how prior HPE art (which performs better with the 300W-LP baseline) would benefit from the suggested training data. In the latter regard, the paper is limited in scope. However, re-training models of prior art would be an interesting direction for future work as it could yield further improvements for HPE and face alignment. Another direction to pursue would be the acquisition of a synthetic dataset like Face Synthetics but with perfect 6 DoF pose labels, abolishing the need to measure the error indirectly via landmark predictions.

As a cautionary tale, the fact that the ResNets lower noise sensitivity only showed when modifying the test set, highlights the risk of "overfitting" methods to a particular test set - in this case with only clean images.

A merit of this work is also the uncertainty estimation with its tangent-space Gaussian formulation which is straight forward to implement, provided an accuracy boost when added to the model, and was effective at detecting failure cases.

On the practical side, both the MobileNet and ResNet variants are accurate, efficient models suitable for real-time applications.

References

- [1] Vitor Albiero, Xingyu Chen, Xi Yin, Guan Pang, and Tal Hassner. img2pose: Face Alignment and Detection via 6DoF, Face Pose Estimation. In *CVPR*, pages 7617–7627, 2021. 6
- [2] Redhwan Algabri, Hyunsoo Shin, and Sungon Lee. Real-time 6DoF full-range markerless head pose estimation. *Expert Systems with Applications*, 239:122293, 2024. 6
- [3] Andrea Asperti and Daniele Filippini. Deep Learning for Head Pose Estimation: A Survey. *SN Comput. Sci.*, 4(4), 2023. 1
- [4] José Celestino, Manuel Marques, Jacinto C. Nascimento, and Jo textasciitilde ao Paulo Costeira. 2D Image head pose estimation via latent space regression under occlusion settings. *Pattern Recognit.*, 137:109288, 2023. 6
- [5] Djork-Arné Clevert, Thomas Unterthiner, and Sepp Hochreiter. Fast and Accurate Deep Network Learning by Exponential Linear Units (ELUs). In *ICCV*, 2016. 2
- [6] Alejandro Cobo, Roberto Valle, José M. Buenaposada, and Luis Baumela. On the representation and methodology for wide and short range head pose estimation. *Pattern Recognition*, 149:110263, 2024. 1, 2, 5, 6
- [7] Radek Daneczek, Michael J. Black, and Timo Bolkart. EMOCA: Emotion Driven Monocular Face Capture and Animation. In *CVPR*, pages 20311–20322, 2022. 4
- [8] Nicola De Cao and Wilker Aziz. The Power Spherical distribution. In *Proc. International Conference on Machine Learning, INNF+*, 2020. 2
- [9] Gabriele Fanelli, Matthias Dantone, Juergen Gall, Andrea Fossati, and Luc Van Gool. Random Forests for Real Time 3D Face Analysis. *Int. J. Comput. Vis.*, 101(3):437–458, 2013. 1
- [10] Yao Feng, Fan Wu, Xiaohu Shao, Yanfeng Wang, and Xi Zhou. Joint 3D Face Reconstruction and Dense Alignment with Position Map Regression Network. In *ECCV*, pages 557–574, 2018. 8
- [11] Yao Feng, Haiwen Feng, Michael J. Black, and Timo Bolkart. Learning an Animatable Detailed 3D Face Model from In-The-Wild Images. In *ACM Transactions on Graphics, (Proc. SIGGRAPH)*, 2021. 4
- [12] Igor Gilitschenski, Roshni Sahoo, Wilko Schwarting, Alexander Amini, Sertac Karaman, and Daniela Rus. Deep Orientation Uncertainty Learning based on a Bingham Loss. In *ICCV*, 2020. 2
- [13] Jinwei Gu, Xiaodong Yang, Shalini De Mello, and Jan Kautz. Dynamic Facial Analysis: From Bayesian Filtering to Recurrent Neural Network. In *CVPR*, pages 1531–1540, 2017. 1
- [14] Jianzhu Guo, Xiangyu Zhu, Yang Yang, Fan Yang, Zhen Lei, and Stan Z. Li. Towards Fast, Accurate and Stable 3D Dense Face Alignment. In *ECCV*, pages 152–168, 2020. 1, 2, 4, 5, 8
- [15] Kaiming He, Xiangyu Zhang, Shaoqing Ren, and Jian Sun. Deep Residual Learning for Image Recognition. In *CVPR*, pages 770–778, 2016. 2

- [16] Thorsten Hempel, Ahmed A. Abdelrahman, and Ayoub Al-Hamadi. 6d Rotation Representation For Unconstrained Head Pose Estimation. In *IEEE International Conference on Image Processing, ICIP, Bordeaux, France*, pages 2496–2500, 2022. 1, 6
- [17] Thorsten Hempel, Ahmed A. Abdelrahman, and Ayoub Al-Hamadi. Toward Robust and Unconstrained Full Range of Rotation Head Pose Estimation. *IEEE Transactions on Image Processing*, 33:2377–2387, 2024. 6
- [18] Andrew G. Howard, Menglong Zhu, Bo Chen and Dmitry Kalenichenko, Weijun Wang, Tobias Weyand, Marco Andreetto, and Hartwig Adam. MobileNets: Efficient Convolutional Neural Networks for Mobile Vision Applications. *CoRR*, abs/1704.04861, 2017. 2
- [19] Heng-Wei Hsu, Tung-Yu Wu, Sheng Wan, Wing Hung Wong, and Chen-Yi Lee. QuatNet: Quaternion-Based Head Pose Estimation With Multiregression Loss. *IEEE Trans. Multim.*, 21(4):1035–1046, 2019. 1, 6
- [20] Du Q. Huynh. Metrics for 3D Rotations: Comparison and Analysis. *J. Math. Imaging Vis.*, 35(2):155–164, 2009. 3
- [21] Pavel Izmailov, Dmitrii Podoprikin, Timur Garipov, Dmitry P. Vetrov, and Andrew Gordon Wilson. Averaging Weights Leads to Wider Optima and Better Generalization. In *Proc. Conference on Uncertainty in Artificial Intelligence, UAI*, pages 876–885, 2018. 5
- [22] Ira Kemelmacher-Shlizerman, Steven M. Seitz, Daniel Miller, and Evan Brossard. The MegaFace Benchmark: 1 Million Faces for Recognition at Scale. In *CVPR*, pages 4873–4882, 2016. 4
- [23] Alex Kendall and Yarin Gal. What Uncertainties Do We Need in Bayesian Deep Learning for Computer Vision? In *NeurIPS*, pages 5574–5584, 2017. 2, 3
- [24] Diederik P. Kingma and Jimmy Ba. Adam: A Method for Stochastic Optimization. In *ICCV*, 2015. 5
- [25] Felix Kuhnke and Jörn Ostermann. Deep Head Pose Estimation Using Synthetic Images and Partial Adversarial Domain Adaption for Continuous Label Spaces. In *ICCV*, pages 10163–10172, 2019. 1
- [26] Felix Kuhnke and Jörn Ostermann. Domain Adaptation for Head Pose Estimation Using Relative Pose Consistency. *IEEE Trans. Biom. Behav. Identity Sci.*, 5(3):348–359, 2023. 1
- [27] Balaji Lakshminarayanan, Alexander Pritzel, and Charles Blundell. Simple and Scalable Predictive Uncertainty Estimation using Deep Ensembles. In *NeurIPS*, pages 6402–6413, 2017. 2, 3
- [28] Taeyoung Lee. Bayesian Attitude Estimation with Approximate Matrix Fisher Distributions on $SO(3)$. In *IEEE Conference on Decision and Control, CDC*, pages 5319–5325, 2018. 2
- [29] Taeyoung Lee. Bayesian Attitude Estimation With the Matrix Fisher Distribution on $SO(3)$. *IEEE Trans. Autom. Control.*, 63(10):3377–3392, 2018. 2
- [30] Heyuan Li, Bo Wang, Yu Cheng, Mohan S. Kankanhalli, and Robby T. Tan. DSFNet: Dual Space Fusion Network for Occlusion-Robust 3D Dense Face Alignment. In *CVPR*, pages 4531–4540, 2023. 1, 6
- [31] Tianye Li, Timo Bolkart, Michael J. Black, Hao Li, and Javier Romero. Learning a model of facial shape and expression from 4D scans. *ACM Transactions on Graphics, (Proc. SIGGRAPH Asia)*, 36(6):194:1–194:17, 2017. 4
- [32] Hai Liu, Shuai Fang, Zhaoli Zhang, Duantengchuan Li, Ke Lin, and Jiazhong Wang. MFDNet: Collaborative Poses Perception and Matrix Fisher Distribution for Head Pose Estimation. *IEEE Trans. Multim.*, 24:2449–2460, 2022. 1, 6
- [33] Yinglu Liu, Hailin Shi, Hao Shen, Yue Si, Xiaobo Wang, and Tao Mei. A New Dataset and Boundary-Attention Semantic Segmentation for Face Parsing. In *Proc. AAAI Conference on Artificial Intelligence*, pages 11637–11644, 2020. 4
- [34] Tetiana Martyniuk, Orest Kupyn, Yana Kurlyak, Igor Krashenyi, Jiri Matas, and Viktoriia Sharmanska. DAD-3DHeads: A Large-scale Dense, Accurate and Diverse Dataset for 3D Head Alignment from a Single Image. In *CVPR*, pages 20910–20920, 2022. 6
- [35] Stephen Milborrow, Tom E. Bishop, and Fred Nicolls. Multiview Active Shape Models with SIFT Descriptors for the 300-W Face Landmark Challenge. In *ICCVW*, pages 378–385, 2013. 2
- [36] David Mohlin, Josephine Sullivan, and Gérald Bianchi. Probabilistic Orientation Estimation with Matrix Fisher Distributions. In *NeurIPS*, 2020. 2
- [37] D.A. Nix and A.S. Weigend. Estimating the mean and variance of the target probability distribution. In *Proc. International Conference on Neural Networks (ICNN)*, pages 55–60 vol.1, 1994. 3
- [38] Pascal Paysan, Reinhard Knothe, Brian Amberg, Sami Romdhani, and Thomas Vetter. A 3D Face Model for Pose and Illumination Invariant Face Recognition. In *IEEE International Conference on Advanced Video and Signal Based Surveillance, AVSS*, pages 296–301, 2009. 2
- [39] Valentin Peretroukhin, Matthew Giamou, W. Nicholas Greene, David M. Rosen, Jonathan Kelly, and Nicholas Roy. A Smooth Representation of Belief over $SO(3)$ for Deep Rotation Learning with Uncertainty. In *Robotics: Science and Systems XVI, Virtual Event / Corvallis, Oregon, USA*, 2020. 2
- [40] René Ranftl, Katrin Lasinger, David Hafner, Konrad Schindler, and Vladlen Koltun. Towards Robust Monocular Depth Estimation: Mixing Datasets for Zero-shot Cross-dataset Transfer. *IEEE Transactions on Pattern Analysis and Machine Intelligence (TPAMI)*, 2020. 4
- [41] René Ranftl, Alexey Bochkovskiy, and Vladlen Koltun. Vision Transformers for Dense Prediction. In *ICCV*, pages 12159–12168, 2021. 4
- [42] Zeyu Ruan, Changqing Zou, Longhai Wu, Gangshan Wu, and Limin Wang. SADRNet: Self-Aligned Dual Face Regression Networks for Robust 3D Dense Face Alignment and Reconstruction. *IEEE Trans. Image Process.*, 30:5793–5806, 2021. 1, 2, 5, 6, 8

- [43] Nataniel Ruiz, Eunji Chong, and James M. Rehg. Fine-Grained Head Pose Estimation Without Keypoints. In *CVPRW*, pages 2074–2083, 2018. 5, 6
- [44] Christos Sagonas, Epameinondas Antonakos, Georgios Tzimiropoulos, Stefanos Zafeiriou, and Maja Pantic. 300 Faces In-The-Wild Challenge: database and results. *Image Vis. Comput.*, 47:3–18, 2016. 2
- [45] Laurens Sluijterman, Eric Cator, and Tom Heskes. Optimal training of Mean Variance Estimation neural networks. *Neurocomputing*, 597:127929, 2024. 3
- [46] Chien Thai, Viet Tran, Minh Bui, Huong Ninh, and Hai Tran. An Effective Deep Network for Head Pose Estimation without Keypoints. In *ICPRAM*, pages 90–98, 2022. 6
- [47] Roberto Valle, José Miguel Buenaposada, and Luis Baumela. Multi-Task Head Pose Estimation in-the-Wild. *IEEE Trans. Pattern Anal. Mach. Intell.*, 43(8): 2874–2881, 2021. 1, 6
- [48] Erroll Wood, Tadas Baltrušaitis, Charlie Hewitt, Sebastian Dziadzio, Thomas J Cashman, and Jamie Shotton. Fake it till you make it: face analysis in the wild using synthetic data alone. In *CVPR*, pages 3681–3691, 2021. 4
- [49] Cho-Ying Wu, Qiangeng Xu, and Ulrich Neumann. Synergy between 3DMM and 3D Landmarks for Accurate 3D Facial Geometry. In *International Conference on 3D Vision, 3DV*, pages 453–463, 2021. 1, 2, 6, 8
- [50] Wayne Wu, Chen Qian, Shuo Yang, Quan Wang, Yici Cai, and Qiang Zhou. Look at Boundary: A Boundary-Aware Face Alignment Algorithm. In *CVPR*, pages 2129–2138, 2018. 4
- [51] Tsun-Yi Yang, Yi-Ting Chen, Yen-Yu Lin, and Yung-Yu Chuang. FSA-Net: Learning Fine-Grained Structure Aggregation for Head Pose Estimation From a Single Image. In *CVPR*, pages 1087–1096, 2019. 5, 6
- [52] Yingda Yin, Yang Wang, He Wang, and Baoquan Chen. A Laplace-inspired Distribution on $SO(3)$ for Probabilistic Rotation Estimation. In *ICCV*, 2023. 2
- [53] Cheng Zhang, Hai Liu, Yongjian Deng, Bochen Xie, and Youfu Li. TokenHPE: Learning Orientation Tokens for Efficient Head Pose Estimation via Transformers. In *CVPR*, pages 8897–8906, 2023. 6
- [54] Hongwen Zhang, Qi Li, and Zhenan Sun. Adversarial Learning Semantic Volume for 2D/3D Face Shape Regression in the Wild. *IEEE Transactions on Image Processing*, 28(9):4526–4540, 2019. 8
- [55] Yijun Zhou and James Gregson. WHENet: Real-time Fine-Grained Estimation for Wide Range Head Pose. In *BMVC*, 2020. 6
- [56] Xiangyu Zhu, Zhen Lei, Xiaoming Liu, Hailin Shi, and Stan Z. Li. Face Alignment Across Large Poses: A 3D Solution. In *CVPR*, pages 146–155, 2016. 1, 2, 4, 7, 8
- [57] Xiangyu Zhu, Xiaoming Liu, Zhen Lei, and Stan Z. Li. Face Alignment in Full Pose Range: A 3D Total Solution. *IEEE Trans. Pattern Anal. Mach. Intell.*, 41(1):78–92, 2019. 2
- [58] Wojciech Zielonka, Timo Bolkart, and Justus Thies. Towards Metrical Reconstruction of Human Faces. In *ECCV*, 2022. 4

A Appendix

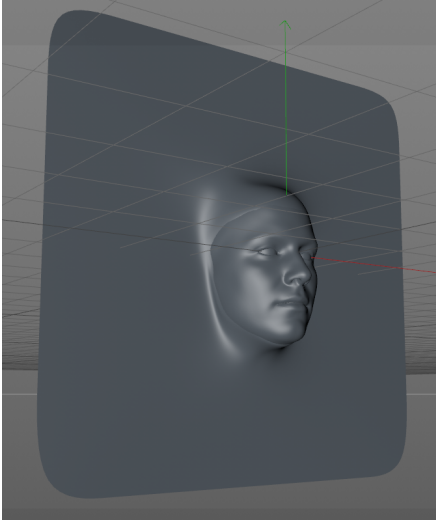


Figure 5. The underlying mesh for rendering images with out-of-plane rotations.

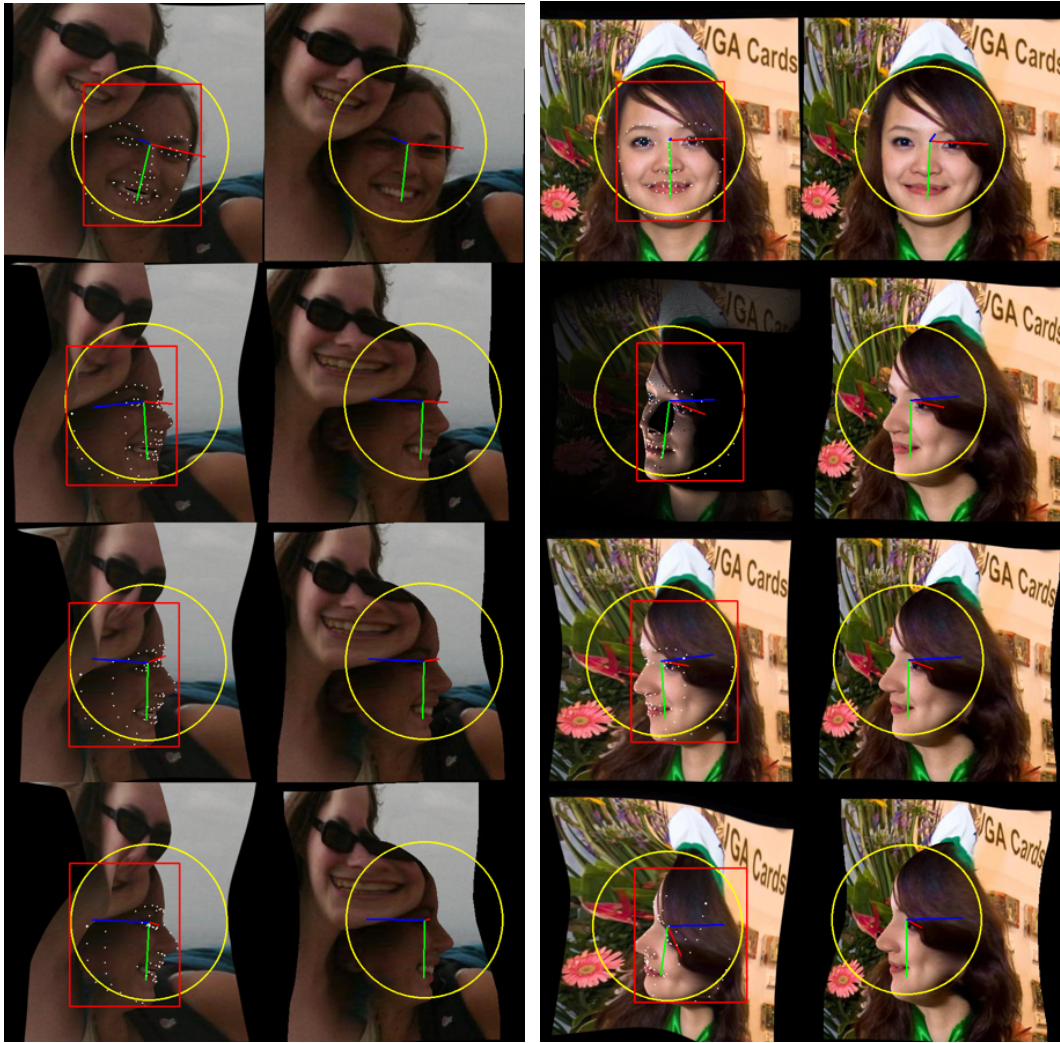


Figure 6. Example frames of the extended 300W-LP dataset. Left and right panel show difference subjects. Per panel, left column: new, right column: 300W-LP.



Figure 7. Example frames from the synthetically expanded LaPa dataset.



Figure 8. Example frames from the synthetically expanded LaPa dataset.

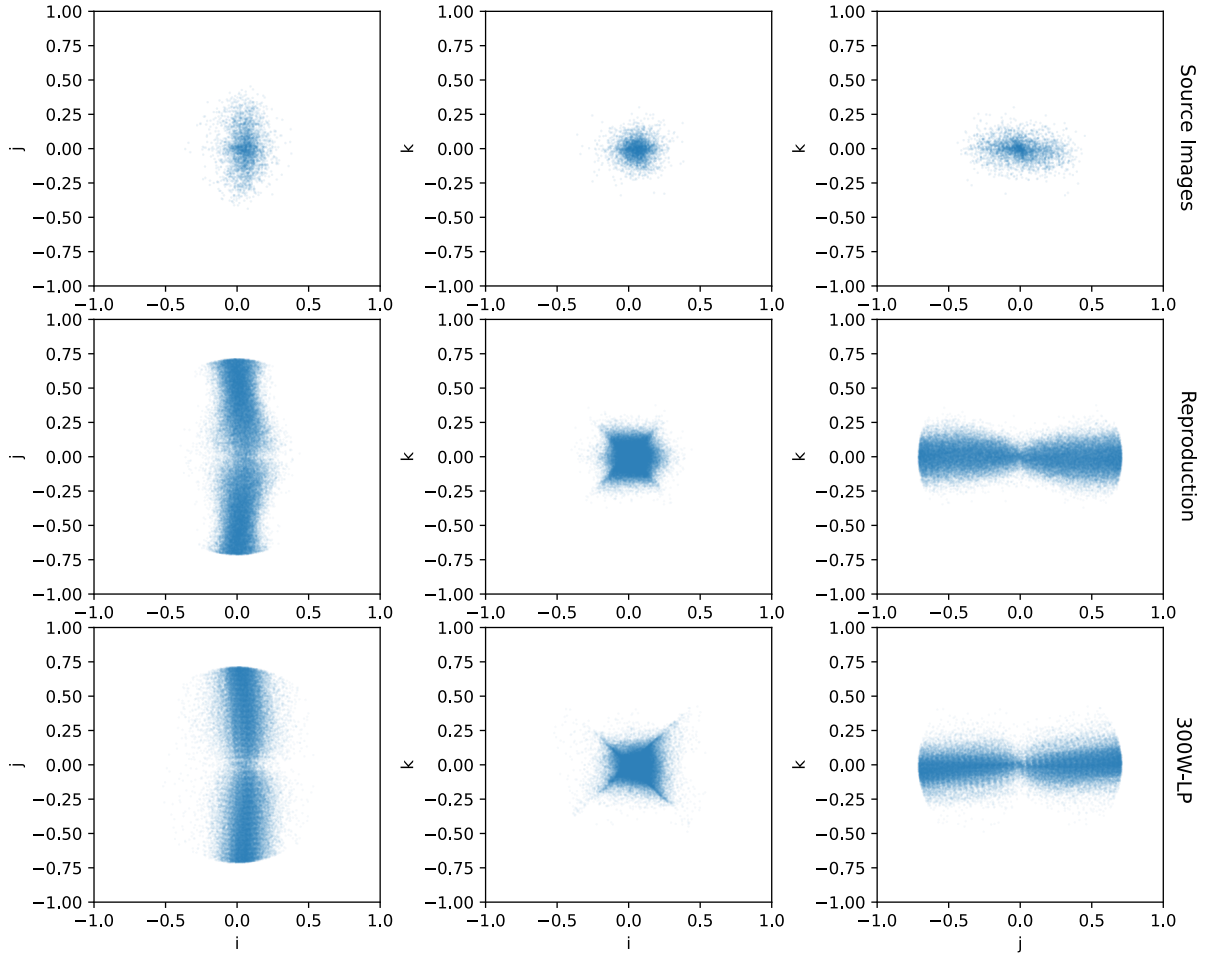


Figure 9. Rotation distribution of the expansion by in-plane rotations. The plots show projections of the quaternion components of the rotation annotations. Every point represents a sample in the respective dataset. Top row: original without expansion. Middle: my reproduction. Bottom: 300W-LP.